A&A 531, A112 (2011)
DOI: 10.1051/0004-6361/201016255

Astronomy & Astrophysics

The continuum intensity as a function of magnetic field

I. Active region and quiet Sun magnetic elements

P. Kobel[1], S. K. Solanki[1,2], and J. M. Borrero[3]

[1] Max-Planck Institut für Sonnensystemforschung, Max-Planck-Straße 2, 37191 Katlenburg-Lindau, Germany
e-mail: philippe.kobel@a3.epfl.ch
[2] School of Space Research, Kyung Hee University, Yongin, 446-701 Gyeonggi, Korea
[3] Kiepenheuer-Institut für Sonnenphysik, Schöneckstr. 6, 79104 Freiburg, Germany

Received 3 December 2010 / Accepted 20 April 2011

ABSTRACT

Context. Small-scale magnetic fields are major contributors to the solar irradiance variations. Hence, the continuum intensity contrast of magnetic elements in the quiet Sun (QS) network and in active region (AR) plage is an essential quantity that needs to be measured reliably.
Aims. By using Hinode/SP disk center data at a constant, high spatial resolution, we aim at updating results of earlier ground-based studies of contrast vs. magnetogram signal, and to look for systematic differences between AR plages and QS network.
Methods. The field strength, filling factor and inclination of the field was retrieved by means of a Milne-Eddington inversion (VFISV code). As in earlier studies, we then performed a pixel-by-pixel study of 630.2 nm continuum contrast vs. apparent (i.e. averaged over a pixel) longitudinal magnetic field over large fields of view in ARs and in the QS.
Results. The continuum contrast of magnetic elements reaches larger values in the QS (on average 3.7%) than in ARs (on average 1.3%). This could not be attributed to any systematic difference in the chosen contrast references, so that it mainly reflects an intrinsic brightness difference. The larger contrasts in the QS are in agreement with earlier, lower resolution results, although our values are larger due to our better spatial resolution. At Hinode's spatial resolution, moreover, the relationship between contrast and apparent longitudinal field strength exhibits a peak at around 700 G in both the QS and ARs, whereas earlier lower resolution studies only found a peak in the QS and a monotonic decrease in ARs. We attribute this discrepancy both to our careful removal of the pores and their close surroundings affected by the telescope diffraction, as well as to the enhanced spatial resolution and very low scattered light of the Hinode Solar Optical Telescope. We verified that the magnetic elements producing the peak in the contrast curve are rather vertical in the AR and in the QS, so that the larger contrasts in the QS cannot be explained by larger inclinations, as had been proposed earlier. The opposite polarities in ARs do not exhibit any noticeable difference in inclination either, although they reach different contrasts when the amount of flux is significantly unbalanced between the polarities.
Conclusions. According to our inversions, the magnetic elements producing the peak of the contrast curves have similar properties (field strength, inclination, filling factor) in ARs and in the QS, so that the larger brightness of magnetic elements in the QS remains unexplained. Indirect evidence suggests that the contrast difference is not primarily due to any difference in average size of the magnetic elements. A possible explanation lies in the different efficiencies of convective energy transport in the QS and in ARs, which will be the topic of a second paper.

Key words. Sun: photosphere – Sun: faculae, plages – Sun: surface magnetism – Sun: activity

1. Introduction

The quiet Sun (QS) network and active region (AR) plages are the two most prominent components of solar photospheric magnetism outside Sunspots (Solanki et al. 2006). Both components contain small-scale magnetic features possessing kG field strengths, which appear bright in spectral line cores and theoretically also at continuum wavelengths, even at disk center (Deinzer et al. 1984; Schuessler & Solanki 1988; Knölker et al. 1988, 1991; Vögler & Schüssler 2003). Their excess brightness is due to the fact that they are hotter than their surroundings at equal optical depth (see Schüssler 1992). Owing to their enhanced brightness, these so-called "magnetic elements" are key players in the total solar irradiance variations on the timescale of days to the solar cycle (Krivova et al. 2003; Domingo et al. 2009) and very likely also longer (Krivova et al. 2007). Yet the observed continuum brightness of magnetic elements in ARs and in the QS is still a matter of debate, as is the relative contribution of ARs and QS network to the total solar irradiance variations (although the variation in area and Ca II K emission of ARs were found to dominate on timescales of a solar cycle, Walton et al. 2003). It is thus fundamental to quantify the continuum brightness of magnetic elements in the QS network and in ARs separately, inasmuch as visible continuum wavelengths contribute ~50% to the total solar irradiance and ~30% to its solar cycle variation (according to the calculations of Krivova et al. 2006).

The brightness of magnetic features is usually not measured in absolute sense, but relative to the mean intensity of a reference quiet photosphere, i.e. by their "contrast". The contrast at continuum wavelengths is thus directly related to the temperature excess with respect to this quiet photosphere at the level $\tau = 1$. At disk center (and generally at any fixed heliocentric angle), the temperature excess of a magnetic feature depends on its field strength, which determines the depth of the opacity depression, and on the effectiveness of the radiative heating from its "hot walls" (Spruit 1976). This latter depends on the size of the flux tube, in particular the ratio of the surface of the walls to the internal volume, as well as on the efficiency of

the surrounding convective heat transport. Since measurements based on line-ratio techniques and inversions indicate similar kG field strengths for magnetic elements in network and plages (with a weak dependence on the filling factor, Frazier & Stenflo 1972; Stenflo 1973; Solanki & Stenflo 1984; Stenflo & Harvey 1985; Zayer et al. 1990; Rabin 1992b,a), the continuum contrast of magnetic elements at disk center should be primarily dictated by their sizes (Spruit & Zwaan 1981). Note that the much weaker equipartition fields detected mostly in the internetwork by, e.g. Lin (1995); Solanki et al. (1996); Lites (2002); Khomenko et al. (2003) and the ubiquitous horizontal fields detected with Hinode (Lites et al. 2008; Ishikawa & Tsuneta 2009) are likely to display a much smaller, possibly unimportant contrast (Schnerr & Spruit 2011). A recent study by Viticchié et al. (2010) also suggests that the contrast of disk center *G*-band bright points, which are associated with magnetic elements, mainly depends on their size while the ~kG field strength is rather constant. Note that the contrast of magnetic elements also increases with the heliocentric angle (with an eventual maximum, see Solanki 1993; Steiner 2007, for reviews), as progressively more of the hot granular wall limbward of the flux tubes becomes visible ("hot wall effect", see e.g. Spruit 1976; Keller et al. 2004) and the optical depth shifts upward where magnetic elements have a larger temperature excess due to the shallower temperature gradient inside than outside the flux tubes (Steiner 2005). Signatures of these hot granular walls ("faculae") can be seen directly in the high resolution continuum and *G*-band images of Lites et al. (2004), Kobel et al. (2009) Hirzberger & Wiehr (2005) and Berger et al. (2007), with results of contrast at various heliocentric angles being presented in the last two papers. While the present paper only deals with disk center data, the center-to-limb variation of the continuum contrast of magnetic elements will be presented in a forthcoming one (Kobel et al., Paper III of this series, in prep.). Finally, as observed by Berger & Title (1996, 2001) and De Pontieu et al. (2006), the contrast of individual magnetic elements is also indirectly a function of time, since both the physical parameters influencing the contrast (magnetic element size, field strength and inclination) and the seeing can vary with time. Thus, the above considerations hold statistically when averaging in time or over an ensemble of magnetic elements. Under these conditions the dependence on the inclination of magnetic elements can be omitted because they are on average close to vertical due to magnetic buoyancy. To indirectly gain information about how the sizes of magnetic elements influence their contrasts at disk center, one can statistically investigate the relation between contrast and "magnetogram signal" (i.e. net longitudinal field in the resolution element obtained from the calibration of Stokes *V*, see Stenflo 2008). Since the kG flux tubes in QS and in AR are rather vertical and have similar field strengths, at a fixed disk position the magnetogram signal should only scale with the fractional area of the resolution element filled by magnetic fields, i.e. the "filling factor". At disk center, this filling factor reflects the total cross section (at the height of line formation) of the magnetic features present in the resolution element.

The easiest and most straightforward way to carry out such an analysis is to make scatterplots of the contrast vs. magnetogram signal (cf. Frazier 1971), and average the contrasts in bins of magnetogram signal. Using this method, Title et al. (1992) and Topka et al. (1992) found that the average continuum contrast (at 676.8, 525, 557.6 and 630.2 nm) of magnetic features in ARs at disk center was negative for all bins of magnetogram signal, i.e. their continuum brightness was never greater than the mean quiet photosphere. To be consistent with the flux tube models predicting intrinsically bright magnetic elements, the authors invoked the effect of limited spatial resolution, smearing the magnetic elements with surrounding dark moats (Title et al. 1992; Topka et al. 1992) and intergranular lanes (Title & Berger 1996). Applying the same method, but on QS network data (of similar resolution), Lawrence et al. (1993) found that the average contrast reaches positive values at magnetogram signals at which the AR contrast was negative. These authors then proposed that the larger contrasts in the QS could be explained by more inclined flux tubes, whereby their bright hot walls would be better visible (Lawrence et al. 1993), but left this hypothesis unverified.

A drawback of the pixel-by-pixel analysis used in the aforementioned works is that it does not preserve the information about individual magnetic features. Instead, the contrast of pixels coming from unrelated features (especially if these features are composed of several pixels) can be assigned to the same bin of magnetogram signal, with the risk of blending information from bright magnetic elements with signals of micropores and intergranular lanes. To focus solely on magnetic elements, an alternative method is to segment the bright features in images and compare the average contrast and magnetogram value for each feature separately (as performed by e.g. Viticchié et al. 2010; Berger et al. 2007). However, the segmentation requires the use of joint high-resolution filtergrams in molecular bands in which the feature contrast is enhanced like the *G*-band or CN band, first used by Sheeley (1969) and Muller & Roudier (1984, see also Zakharov et al. 2007; Uitenbroek & Tritschler 2006, for comparative studies of both bands based on observations and simulations, respectively). Moreover, the segmentation necessarily relies on some arbitrary thresholds, unlike the pixel-by-pixel method. Note that the two methods yield distinct results also because the population of magnetic features they study are different: since the segmentation-based method only selects bright magnetic features, the resulting contrast vs. magnetogram signal curves tend to increase monotonically or reach saturation (Viticchié et al. 2010; Berger et al. 2007). In contrast, due to the inclusion of all pixels, the contrast curves obtained by the second method rather exhibit a peak followed by a decrease due to larger and darker magnetic features (e.g. Fig. 2 herein).

In this paper we compare the 630.2 nm continuum contrast of magnetic elements in ARs and in the QS, using data from the spectropolarimeter onboard Hinode, which allow good determinations of the magnetic field vector and have higher spatial resolution (with constant image quality) than the data of Topka and colleagues (see above). For a direct comparison with their studies we use the same pixel-by-pixel analysis method. We first repeat scatterplots of continuum contrast vs. longitudinal magnetic field in ARs and in the QS, as presented Sect. 3.1. In Sect. 3.2 we compare the inclinations of magnetic elements in the AR and the QS to test the hypothesis of Lawrence et al. (1993), while in Sect. 3.3 we also look for contrast and inclination differences between the opposite polarities in ARs. We then check in Sect. 3.4 that the results are not biased by a systematic difference between the contrast references in ARs and in the QS. Finally, in Sect. 3.5 we explain the qualitative discrepancies between our scatterplots in ARs and those of previous studies. Our conclusions are presented and discussed in Sect. 4.

2. Dataset analysis

2.1. Hinode/SP scans

We selected an ensemble of 6 spectropolarimetric scans over active regions and 4 scans over the quiet Sun performed very close

Table 1. List of the SP scans used in this work. t_{start} denotes the starting time of the scans.

Date (dd-mm-yy)	t_{start} (UT)	Target	NOAA
11-12-06	13:10:09	AR	10930
05-01-07	11:20:09	AR	10933
01-02-07	12:14:05	AR	10940
28-02-07	11:54:34	AR	10944
01-05-07	21:00:06	AR	10953
11-05-07	12:35:53	AR	10955
10-03-07	11:37:36	QS	–
23-04-07	11:14:06	QS	–
24-04-07	01:21:04	QS	–
27-04-07	08:50:03	QS	–

to disk center (see Table 1) by the Hinode/SP instrument (Lites et al. 2001; Ichimoto et al. 2008; Kosugi et al. 2007; Tsuneta et al. 2008; Suematsu et al. 2008).

The SP delivers profiles of the four Stokes parameters (for every pixel along its slit) in a visible wavelength range covering both the Fe I 630.15 nm and 630.25 nm lines, at a constant spatial resolution of 0.″3 (see e.g. Lites et al. 2008, for more details).

The selected scans were performed in the "normal mode", i.e. with an exposure time of 4.8 s resulting in typical rms noise levels at disk center of 1.1×10^{-3} and 1.2×10^{-3} for Stokes V and Q, U, respectively (in units of continuum intensity I_c). All the profiles were calibrated via the `sp_prep` routine of the SolarSoft package[1]. Note that although the point spread function of the SOT/SP has been calculated by Danilovic et al. (2008), no inversions of this function are currently available so that the calibrated data were not further processed.

2.2. Maps of continuum intensity and heliocentric distance

Maps of the continuum intensity I_c (calculated in the red continuum of the 630.2 nm line) were provided by the `sp_prep` procedure. Because of the short exposure times compared to the granulation lifetime (~10 min), these continuum maps can be thought of as quasi-instantaneous images over small distances (cf. Lites et al. 2008). They are thus appropriate for the study of small-scale magnetic features, whose evolution timescales are roughly comparable with those of the granulation (Berger & Title 1996; Berger et al. 1998).

`sp_prep` also calculates the right ascension x and declination y (heliocentric cartesian coordinates), and thereby the $\mu = \cos\theta$ value at each pixel of the maps (where θ is the heliocentric angle). In the present study, these "μ maps" were used to select portions of the scans located at the very disk center, i.e. where $\mu > 0.99$. Only these portions are studied here.

No correction of I_c for limb darkening was performed, as the latter can be estimated to only ~0.05% between $\mu = 1$ and $\mu = 0.99$ (using the 5th-order polynomial in μ published by Neckel & Labs 1994), and therefore is considered negligible.

2.3. Inversions

The observed Stokes spectra at each spatial pixel were inverted with the VFISV (Very Fast Inversion of the Stokes Vector) code of Borrero et al. (2010). We refer to this article for all details. This code produces synthetic Stokes profiles of the 630.2 nm line using the Milne-Eddington solution (M-E) for the radiative transfer equation (see,e.g., del Toro Iniesta 2003), as follows:

$$\boldsymbol{I}^{\rm syn}(\lambda) = \alpha \boldsymbol{I}_{\rm mag}(\lambda, \mathcal{X}) + (1-\alpha)\boldsymbol{I}_{\rm nmag}(\lambda), \quad (1)$$

where $\boldsymbol{I}_{\rm mag}(\lambda, \mathcal{X})$ refers to the Stokes vector arising from the magnetized part of the pixel. Thus, the set of parameters $\mathcal{X}$ refers to the physical properties of the magnetized plasma which, under the M-E approximation, are:

$$\mathcal{X} = [S_0, S_1, \eta_0, a, \Delta\lambda_D, B, \gamma, \phi, v_{\rm los}, \alpha], \quad (2)$$

where the first 5 are the thermodynamic parameters: source function, S_0, source function gradient, S_1, ratio of the absorption coefficient between the continuum and line-center, η_0, damping parameter a, and Doppler width, $\Delta\lambda_D$[2]. The next three refer to the three components of the magnetic field vector: intrinsic field strength, B, inclination of the magnetic field vector with respect to the observer γ, and azimuthal angle in the plane perpendicular to the observer's, ϕ. $v_{\rm los}$ denotes the line-of-sight (LOS) velocity of the magnetized plasma. Finally, the "filling factor" α is a geometrical parameter that refers to the fractional amount of light that corresponds to the magnetized plasma.

To retrieve α, we adopted the "local stray light" approach used by Orozco Suárez et al. (2007; see also Borrero & Kobel 2011). $\boldsymbol{I}_{\rm nmag}(\lambda)$ refers to the Stokes vector arising from the non-magnetized portion of the pixel, and therefore we consider it not to be polarized: $\boldsymbol{I}_{\rm nmag}(\lambda) = (I_{\rm nmag}, 0, 0, 0)$. $I_{\rm nmag}$ is obtained by averaging the intensity profiles from the neighboring pixels within 1″ of the inverted one. Note that, because of the way it is constructed, $I_{\rm nmag}$ cannot distinguish between non-magnetized plasma within the resolution element, the effects of the telescope diffraction and the scattered light within the instrument. However, given the small amount of scattered light in Hinode's spectropolarimeter (Danilovic et al. 2008) the last contribution can be neglected.

We have observationally determined that the noise for Stokes I is typically between a factor of 5 and 10 larger than in Q, U or V due to the flatfield correction (Lites, priv. comm.), which is only known to the order of 1%. To account for that, Stoke I was given 5 times lower weight than the polarization profiles in the inversion scheme.

All the pixels were inverted (no polarization selection) and included in the analysis, as the latter mainly deals with the longitudinal component of the field, which can be considered reliable over the range corresponding to the magnetic elements having Stokes V signal largely above the noise (see Sect. 3.1).

In contrast to older studies using magnetograms (see Sect. 1), the present approach has the advantage of remaining valid in all regimes of intrinsic field strength, as it is based on analytically solving the full radiative transfer equation. Magnetograms rely on a calibration of Stokes V (cf. Topka et al. 1992) that only holds in the "weak field regime", and thus the values of the magnetogram signal are underestimated for vertical fields approaching 1000 G in intrinsic strength (Landi Degl'Innocenti & Landolfi 2004), which is the so-called "Zeeman saturation effect" (Howard & Stenflo 1972; Stenflo 1973).

[1] http://www.lmsal.com/solarsoft/sswdoc/index_menu.html

[2] Note that a was maintained at a prescribed value.

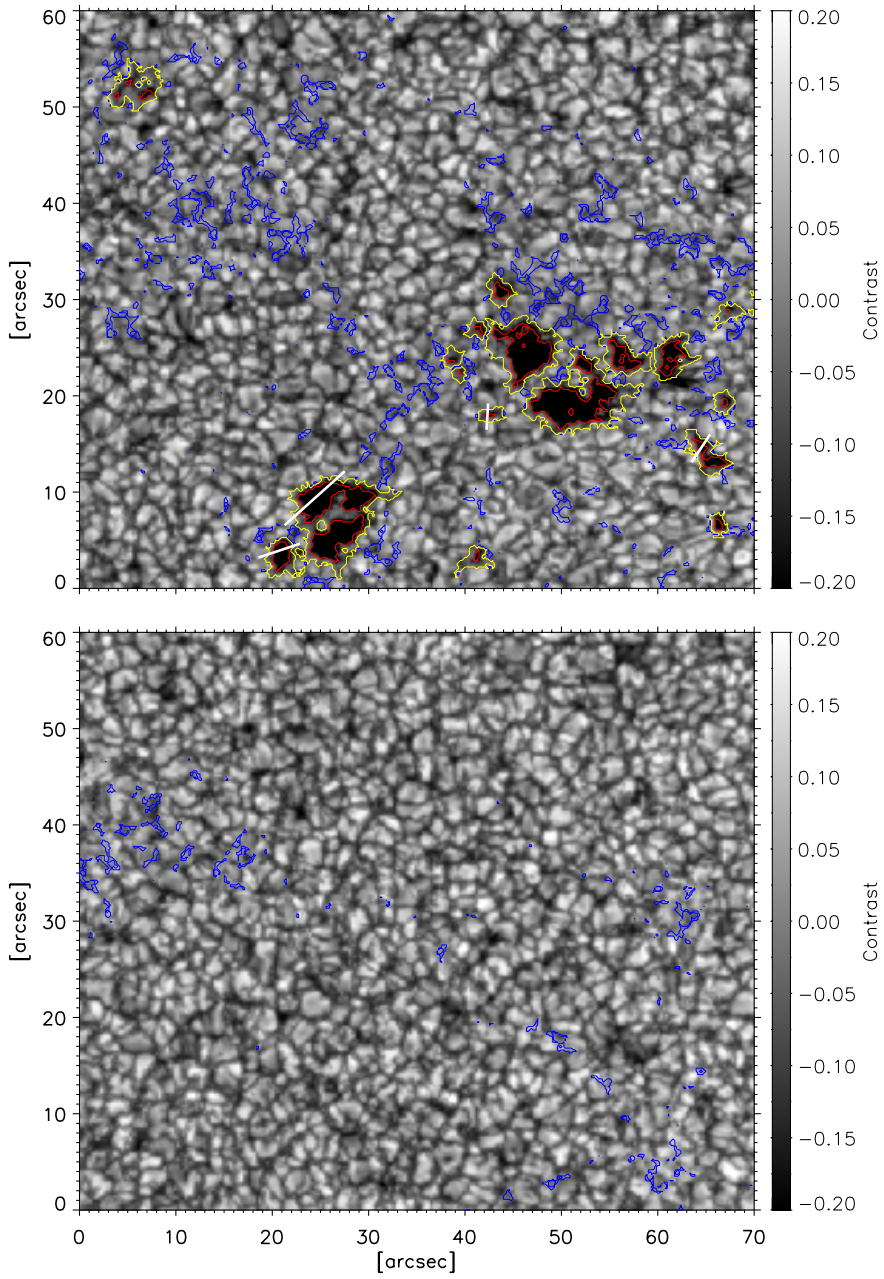

Fig. 1. *Upper panel*: continuum contrast of an active region plage field of view at disk center ($\mu > 0.99$), extracted from the SP scan of day 01-02-2007 (see Table 1). *Bottom panel*: same for a field of view including quiet Sun network, extracted from the SP scan of day 24-04-2007. Blue contours: locations of the pixels where $B_{\rm app,los}$ lies in an interval of ±200 G around the peak value of the contrast vs. $B_{\rm app,los}$ relation (see Fig. 2). The red contours surround the "core" of the pores where the contrast is below −0.15 and $B_{\rm app,los} > 900$ G, while the yellow contours outline the entire pore areas removed from the analysis. The white lines across some pores coincide with the locations of the cuts discussed in Sect. 3.5.

3. Results

3.1. Scatterplots of contrast vs. longitudinal field for active region and quiet Sun

To start with, we performed a pixel-by-pixel comparison of continuum contrast vs. longitudinal field (as undertaken by Title et al. 1989; Topka et al. 1992; Lawrence et al. 1993, hereafter TTL) over active regions (ARs) and the quiet Sun (QS), to see if and how the results would differ between these two targets at the constantly high spatial resolution of Hinode.

Like TTL, we considered rather large fields of view (FOVs) of 70″×60″. We analyzed a total of 10 FOVs containing QS network and 9 FOVs of AR plages, all at $\mu > 0.99$, extracted from the different SP scans (see Sect. 2.1). As we obtained similar results with all FOVs (summarized in Table 2), we restrict ourselves here to presenting the results for one such FOV centered on an AR plage (see Fig. 1 upper panel), and one including QS network (Fig. 1 lower panel).

To simulate the magnetogram signal used by TTL, we considered the "apparent" strength of the longitudinal component of the field $B_{\rm app,los} = B\alpha|\cos\gamma|$ (see Sect. 2.3 for the description of the variables B, α and γ). Like the magnetogram signal, it can be considered to scale with the size of unresolved magnetic elements (see Sect. 1). We use the terminology "apparent" field strength to distinguish from the intrinsic one, since $B_{\rm app,los}$ is averaged over the pixel. The continuum contrast at each pixel location (x, y) of a given FOV was defined as:

$$\text{Contrast}(x,y) = \frac{I_{\rm c}(x,y) - \langle I_{\rm c}\rangle_{\rm ref,FOV}}{\langle I_{\rm c}\rangle_{\rm ref,FOV}}, \quad (3)$$

where $\langle I_{\rm c}\rangle_{\rm ref,FOV}$ is the contrast reference, taken as the mean continuum intensity of the pixels having $B_{\rm app,los} < 100$ G in the FOV (corresponding to rather normal granulation).

Table 2. List of the different fields of view (FOVs) analyzed in this work, extracted from the SP scans indicated by their date (see Table 1).

FOV index	Date (dd-mm-yy)	Target	Contrast peak	$B_{\rm app,los}$ peak [G]	$\langle B\rangle$ [G]	$\langle\alpha\rangle$	$\langle\gamma\rangle$ [°]
1	11-12-06	AR	0.013	677	1104	0.64	15.9
2	05-01-07	AR	0.015	694	1128	0.64	17.2
3	05-01-07	AR	0.027	711	1125	0.64	14.7
4	*01-02-07	AR	0.005	685	1142	0.63	20
5	01-02-07	AR	0.013	711	1147	0.64	17.5
6	28-02-07	AR	0.018	694	1136	0.63	16.1
7	01-05-07	AR	0.008	668	1119	0.62	17.1
8	01-05-07	AR	0.005	668	1106	0.62	16.5
9	11-05-07	AR	0.016	651	1111	0.62	18.7
			0.013	**681**	**1124**	**0.63**	**17.4**
10	10-03-07	QS	0.056	750	1166	0.6	9.7
11	10-03-07	QS	0.029	709	1137	0.61	12.3
12	10-03-07	QS	0.037	678	1096	0.6	9.5
13	23-04-07	QS	0.013	660	1091	0.6	13.2
14	23-04-07	QS	0.046	805	1208	0.63	10.3
15	*24-04-07	QS	0.029	702.5	1142	0.62	12.8
16	24-04-07	QS	0.062	725	1174	0.6	13.5
17	27-04-07	QS	0.04	711	1113	0.63	12.4
18	27-04-07	QS	0.029	702	1122	0.63	12.5
19	27-04-07	QS	0.033	727	1146	0.63	13.1
			0.037	**717**	**1140**	**0.62**	**11.9**

Notes. The AR and QS FOVs described in Sect. 3.1 have their date marked by an asterisk. When several FOVs are extracted from the same scan they share the same date. All these FOVs have sizes of $70'' \times 60''$, except for the dates 11-12-06 and 05-01-07 for which the FOVs are $40'' \times 90''$ and $45'' \times 91''$, respectively. The "Contrast peak" refers to the maximum of the fit of continuum contrast vs. $B_{\rm app,los}$ and "$B_{\rm app,los}$ peak" is the corresponding $B_{\rm app,los}$ at the peak. $\langle B\rangle$, $\langle\alpha\rangle$, $\langle\gamma\rangle$ are calculated over the pixels having $B_{\rm app,los}$ in a ±200 G interval centered around the peak value of $B_{\rm app,los}$. The rows with bold characters indicate the average values of the different quantities for the AR (middle row) and QS FOVs (last row), respectively.

Figure 2 displays the resulting scatterplots of the continuum contrast vs. $B_{\rm app,los}$ for the AR and for the QS FOVs shown in Fig. 1. To prevent pores from contaminating the contrasts in this range, we removed them according to the following procedure. First, their inner dark cores were detected as any group of at least 4 pixels (the minimum number corresponding to spatial resolution) having contrast below −0.15 and $B_{\rm app,los} > 900$ G (assuming pores to be resolved and thus with fields close to kG), such as enclosed by the red contours in Fig. 1. Next, the surroundings of the pores suffering from spurious magnetic signal due to the telescope diffraction (see Sect. 3.5) were also eliminated by spatially extending the detected cores until $B_{\rm app,los}$ drops below 200 G, which corresponds to the larger yellow contours in Fig. 1. This is a conservative procedure, which might assign somewhat too many pixels to pores, but importantly for our work, it ensures that no pixels influenced by a pore's magnetic field are accidently assigned to magnetic elements.

To detect a trend within the scatterplots, the pixel contrasts were averaged into bins of $B_{\rm app,los}$ (with a binwidth of 25 G), and a third-order polynomial was fitted to the average values of $B_{\rm app,los}$ between 200 G and 1000 G[3]. In these scatterplots, one can notice the large contrast scatter for $B_{\rm app,los} \sim 0$ due to granulation, while the scatter and the average contrasts decrease at the same time that the field concentrates in intergranular lanes (see Schnerr & Spruit 2011, for more details on this part). For the range $B_{\rm app,los} > 200$ G, dominated by flux concentrations, the average contrast increases in both plots until reaching a peak for some value of $B_{\rm app,los}$, corresponding to the maximum of the fits. For values of $B_{\rm app,los}$ below the peak value, the features are on average less bright than the peak contrast, either because their field strength is too low or because they are partially unresolved. For $B_{\rm app,los}$ larger than the peak value, the features become progressively darker as the filling factor increases. Note that unlike our trends, all the trends of TTL in ARs are monotonically decreasing. As explained in the Sect. 3.5, this is not only due to our higher spatial resolution but mainly to our complete removal of pores.

Two qualitative observations can be made. Firstly, both the trends of the contrast vs. $B_{\rm app,los}$ in the QS and in AR peak at a similar value $B_{\rm app,los} \sim 700$ G, as indicated by the arrows in Fig. 2 (and listed in Table 2 for all the FOVs analyzed), whereas the AR trends of TTL were monotonically decreasing. Secondly, even at Hinode's constant and high spatial resolution, the QS network reaches larger continuum contrasts than in AR plage, in agreement with the findings of TTL. The average of the peak contrasts in the QS FOVs is 3.7% and 1.3% in the AR FOVs, corresponding to a relative difference of 2.4%. Note that due to our higher spatial resolution (about twice higher than that of TTL, see Sect. 3.5), the average contrasts reported here are larger than the ones measured by TTL: our QS peak contrast reaches almost 3% (and up to 6.2% in other FOVs, see Table 2), twice as high as the value measured by Lawrence et al. (1993) and our AR peak contrast reaches 0.5% or larger (cf. Table 2), whereas TTL's average contrasts in ARs were negative for all bins of magnetogram signal.

We checked that the dominant majority of the pixels distributed around the peak of the trends, i.e. with $B_{\rm app,los}$ in an interval of ±200 G centered on the peak value (between dashed lines in Fig. 2), are relatively well located in intergranular lanes (see contours in Fig. 1), as expected for magnetic elements, or oftentimes surround larger darker features. The probability density function (PDF) of the *intrinsic* field strength B of these pixels reveals that they harbour kG fields in the AR and in the QS, with

[3] We consider that $B_{\rm app,los}$ is reliably retrieved in the range $B_{\rm app,los} > 200$ G, as more than 99.9% of the pixels in that range have a Stokes V amplitude above 4.5 times the rms noise level.

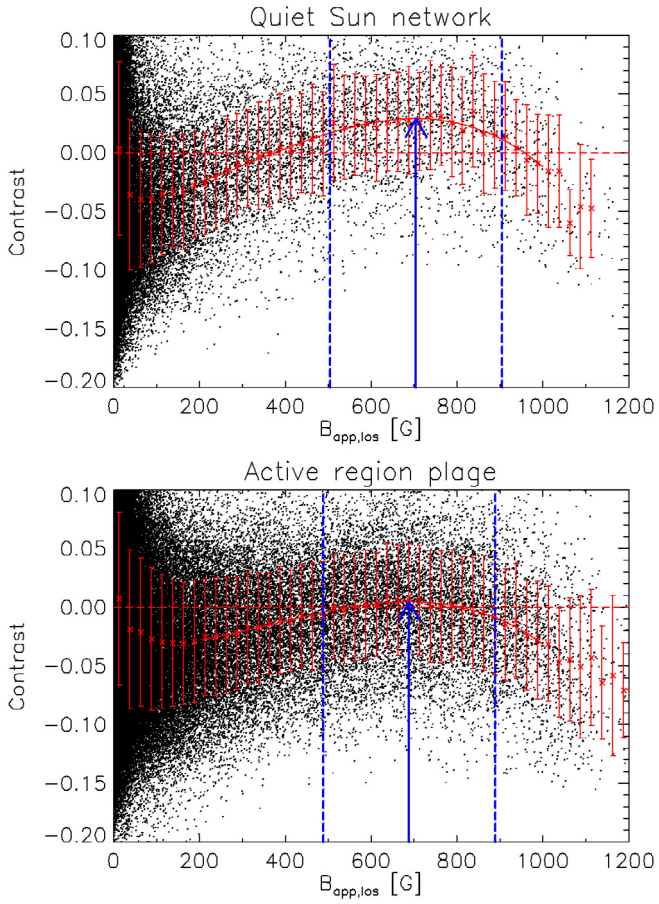

Fig. 2. Scatterplot of the continuum contrast vs. apparent longitudinal field strength $B_{\rm app,los}$ for the quiet Sun (*upper panel*) and plage (*bottom panel*) fields of view shown in Fig. 1, pores excluded. The contrast reference (indicated by the horizontal dashed red line) is the mean intensity of the pixels where $B_{\rm app,los} < 100$ G. Red crosses: average values of the continuum contrast inside $B_{\rm app,los}$-bins of 25 G width. The red error bars are the standard deviations inside each bin. Solid red curves are third-order polynomial fits of the average values in the range 200 G $< B_{\rm app,los} <$ 1000 G. The blue arrows indicate the maxima of the fits, locating the "peak" of the contrast trends. The vertical dashed lines delimit the interval ±200 G around the peak.

nearly the same mean value $\langle B\rangle$ of approx. 1150 G (see Fig. 3a). Since the peak of the contrast trends occurs at similar $B_{\rm app,los}$ for ARs and the QS, the corresponding magnetic elements should also have similar filling factors α (unless their inclination deviates significantly from the vertical), as verified by the PDF(α), which have mean values $\langle\alpha\rangle$ of 0.63 and 0.62 in the AR and in the QS, respectively (Fig. 3b). Assuming that the filling factor scales with the size of the magnetic elements (see Sect. 4), this in turn poses the problem of how to explain their different contrast in the QS and in ARs. As summarized in Table 2, repeating the same analysis on different FOVs of QS and ARs yielded the same conclusions.

3.2. Inclination of the magnetic elements

Based on their observed center-to-limb variation of continuum contrast, Topka et al. (1992) deduced that the contrast of magnetic elements should be sensitive to the angle between the line-of-sight (LOS) and the magnetic lines of force, which at disk center directly translates into their inclination with respect to the local vertical. Lawrence et al. (1993) then proposed that the larger contrasts in the quiet Sun could be explained by a larger inclination of the magnetic elements, whereby their hot walls would be more visible.

We have ruled out this possibility by studying the probability density functions (PDFs) of the inclination γ for the pixels identified with magnetic elements having $B_{\rm app,los}$ in a ±200 G interval around the peak value of the contrast curves (between dashed lines in Fig. 2). Note that in this interval of $B_{\rm app,los}$, all the pixels have a Stokes V amplitude larger than 30 times the rms noise level, while 40% of these pixels also have Q, U amplitudes above 4.5 times their noise level. Figure 3c displays the PDF(γ) for the AR plage and QS FOVs shown in Fig. 1[4]. The magnetic elements are close to vertical in both cases, with a distinctly larger γ in the AR , $\langle\gamma\rangle = 19.9 \pm 0.1°$ (assuming Gaussian statistics), than in the QS, $\langle\gamma\rangle = 12.8 \pm 0.1°$. Probing different FOVs yielded similar PDFs and mean inclinations (see Table 2). Hence, the argument of Lawrence et al. (1993) does not hold. Instead of larger inclinations in the QS, the mean inclinations are systematically (although marginally) larger by 3° to 10° in the AR FOVs. The similarity in the PDFs of B and α strongly argues against a bias responsible for the different inclinations. A check at the inclination maps revealed that these larger inclinations in the ARs mostly occur at the periphery of pores and of dense groups of magnetic features typical of plages, while more isolated magnetic elements like in the QS tend to be more vertical. This is expected as larger flux concentrations like pores have larger vertical expansion rates, which tends to bend the file lines of neighboring magnetic elements. Likewise, a magnetic element located at the periphery of a closely packed group of magnetic features feels a net bending force towards the outside of the group.

Hence, up to the small difference in inclination discussed above, from Fig. 3 and Table 2 we can conclude that all quantities (B, α, γ) have rather similar values for the brightest magnetic elements in the QS and in ARs, which still leaves unexplained the fact that they reach larger contrasts in the QS compared to ARs.

3.3. Positive and negative polarity fields in ARs

So far, we have only dealt with the *strength* of the longitudinal magnetic field without considering the different polarities in the fields of view (FOVs), mainly because our AR FOVs are generally dominated by a single polarity.

However, it is possible that in ARs the contrast of the two opposite polarities differ due to their possible interaction and/or different inclination of their magnetic elements. For instance, cases of Moving Magnetic Features (MMFs) in a Sunspot moat have been reported to interact with the opposite polarity magnetic elements yielding chromospheric surges in Hα (Brooks et al. 2007). Such interacting features could exhibit different contrasts, possibly related to different inclinations (following the argument of Topka et al. 1992, see Sect. 3.2). When analyzing the continuum contrast vs. magnetogram signal separately of the two polarities, Topka et al. (1992) found a difference between the contrasts reached by the two polarities (with either the positive or negative polarity being brighter depending on the FOV), for different instances of AR plages located at heliocentric angles $\theta = 4, 7$ and 43°. They concluded that this angle had to be different between the two polarities (employing the same reasoning as

[4] As we are here only interested in quantifing the deviation from the vertical, all the inclinations γ are reported in the range $0° < \gamma < 90°$.

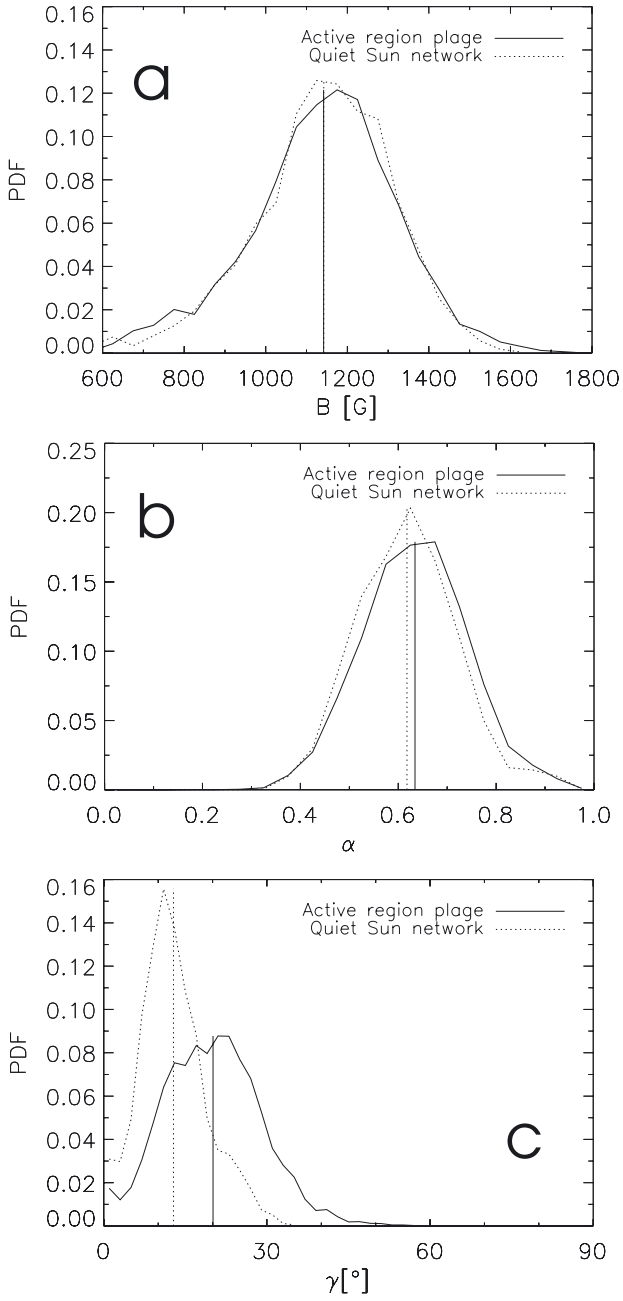

Fig. 3. Probability density functions (PDFs) of **a)** the intrinsic field strength, B, **b)** the magnetic filling factor, α and **c)** the inclination γ of the pixels having $B_{\rm app,los}$ in an interval of ±200 G around the peak value of $B_{\rm app,los}$, for the quiet Sun (dotted curves) and the active region (solid curves) fields of view shown in Fig. 1. The vertical lines mark the mean values of the distributions.

Lawrence et al. 1993, to explain the different contrasts between QS network and AR plage, see Sect. 3.2).

In six cases, our ARs FOVs contained enough flux of both polarities to investigate their behaviour separately. We present here one example, while we list the results obtained from the other five FOVs in Table 3. Figure 4 shows a map of the "signed $B_{\rm app,los}$" (i.e. the longitudinal component of the apparent magnetic field) saturated at ±100 G, to illustrate the distribution of the patches of both polarity fields in the example FOV (positive in white, negative in black). In fact, the minority (negative) polarity is essentially distributed close to the Sunspot (on the immediate right out of the FOV) and probably corresponds to footpoints of magnetic field lines from the penumbra. Repeating the pixel-by-pixel analysis of contrast vs. $B_{\rm app,los}$ for both polarities as in Fig. 5 reveals that, although the contrasts peak at $B_{\rm app,los} \sim 700$ G for both polarities, the minority polarity reaches larger contrasts by almost 3%. However, the probability distribution function of the inclination γ for the pixels with $B_{\rm app,los}$ in an interval of ±200 G around the contrast peaks of each polarity (blue and cyan contours in Fig. 4, associated with the magnetic elements producing the contrast peak) does not show any noticeable difference between both polarities, as visible in Fig. 5 (lower panels). As one can see in Table 3, in none of the six FOVs does the mean inclination $\langle\gamma\rangle_{\pm}$ of the magnetic elements differ between the positive (+) and negative (−) polarity, although the peak contrasts differ by 0.1 to 3.9%. Thus, the observed contrast difference between polarities can not be accounted for by different inclinations.

We noticed that the peak contrast was always larger in the minority polarity and that in general, the contrast difference between polarities was larger for FOVs in which the polarities were seemingly more "unbalanced" (i.e. the ratio of surface coverage between majority and minority polarity was larger). To quantify this, we calculated the fraction of the total unsigned flux carried by each polarity as:

$$X_{\pm} = \frac{\int_{\rm FOV_{\pm}} {\rm d}A_{\pm} B_{\rm app,los}}{\int_{\rm FOV} {\rm d}A B_{\rm app,los}}, \tag{4}$$

where the integration $\int_{\rm FOV_{\pm}}$ is performed over those areas covered by the positive or negative polarity. Note that pores were included in this calculation. In the three cases where the majority polarity carries >70% of the flux (labeled by superscript "a" in Table 3), the peak contrast of the majority polarity is systematically significantly lower than that of the minority polarity by 1.3 to 3.9%. In one exception (labeled "b"), although the majority polarity contains twice as much flux as the minority polarity, the peak contrast of the majority polarity is only marginally lower. For the remaining two cases where the fluxes were rather balanced (labeled "c"), the peak contrasts are very similar in one case but differ by about 3% in the other one (FOV index 9 in the table). This specific FOV differs from all the others in that it harbours the only small bipolar ephemeral region in our dataset, while all the other FOVs contain plage areas in the vicinity of sunspots. Moreover, a look at the full scan containing this FOV reveals that the positive polarity is in fact by far dominating, but that most of its flux is located outside of the selected FOV (the rest of the area was not selected since it lays at $\mu < 0.99$).

We propose that the lower contrast of the predominant polarity is explained by the larger size of its magnetic field patches (saturated white in Fig. 4). These represent larger obstacles to the convective flows and thereby are prone to contain cooler magnetic elements, whereas the patches of the minority polarity are rather reminiscnent of the QS network. The influence of such magnetic patches on the surrounding convection will be presented in more details in a forthcoming paper (Kobel et al., Paper II of this series, in prep.).

3.4. Intrinsic brightness of the magnetic elements

One possibility to explain the lower contrast of magnetic elements in ARs compared to the QS is that the absolute brightness of the chosen contrast reference $\langle I_{\rm c}\rangle_{\rm ref,FOV}$ (mean continuum intensity of the pixels having $B_{\rm app,los} < 100$ G in the FOV, see Eq. (3)) is systematically larger in ARs compared to the QS,

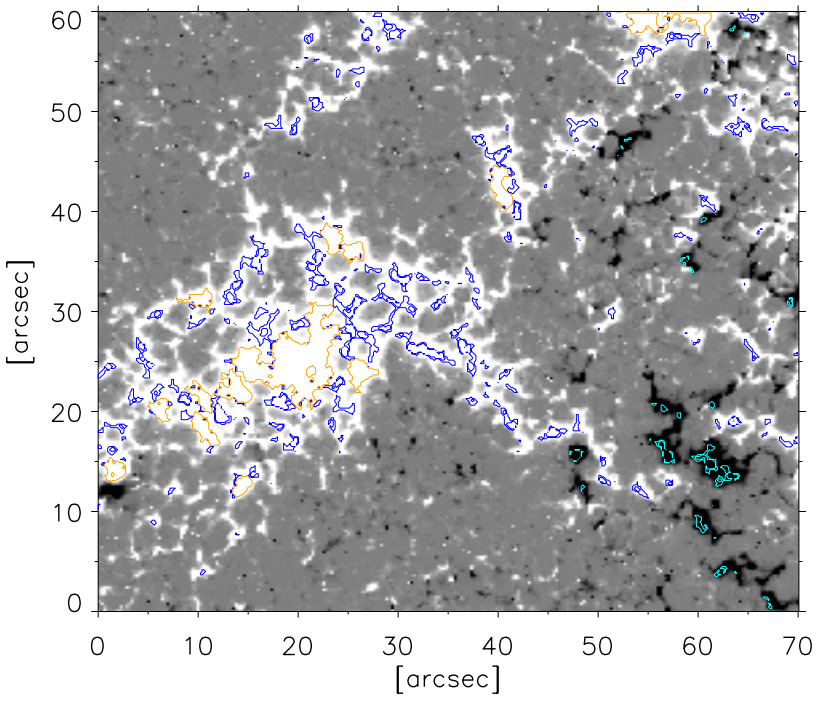

Fig. 4. Map of "signed $B_{\rm app,los}$" for the AR FOV extracted from the SP scan dated 01-02-07 (FOV index 5, see Table 2. The map is saturated at +100 G (white) and −100 G (black). The pores eliminated from the contrast analysis are contoured in orange (there is no pores in the negative polarity). The pixels having $B_{\rm app,los}$ in an interval of ±200 G around the contrast peaks of each polarity are contoured in blue (positive polarity) and cyan (negative polarity).

Table 3. Values of peak contrast, mean inclination $\langle\gamma\rangle_{\pm}$ and fraction of the total unsigned flux $X_{\pm}$ in the positive (+) and negative (−) polarities for the AR FOVs analyzed in Sect. 3.3.

FOV index	Contrast peak (+)	Contrast peak (−)	$\langle\gamma\rangle_+$ [°]	$\langle\gamma\rangle_-$ [°]	X_+	X_-
*5[a]	0.009	0.036	17.8	164.5	90.5	9.5
6[a]	0.015	0.054	16	166.7	89.5	10.5
1[a]	0.024	0.011	16.4	164.5	27.7	72.3
2[b]	0.017	0.013	17.2	162.4	32.3	67.7
3[c]	0.027	0.026	15.2	166	53.5	46.5
9[c]	0	0.029	18	160	53.6	46.4

Notes. The FOV index is the same as in Table 2. The example FOV presented in Figs. 4 and 5 has and asterisk before its index. $\langle\gamma\rangle_{\pm}$ was calculated only for the pixels distributed in an interval of ±200 G around the $B_{\rm app,los}$ location of the contrast peak in each polarity.

such as to account for the relative difference of 2.4% in the average peak contrasts (see Sect. 3.1 and Table 2). This hypothesis is a priori supported by the idea of global horizontal convective inflows developing towards ARs to compensate for the radiative losses through the magnetic atmosphere (Komm et al. 1993; Spruit 2003; Zhao & Kosovichev 2004; Rempel 2006), in a similar fashion as in the case of the case of simple 2D flux sheets (Deinzer et al. 1984). A possible opacity reduction of the magnetic atmosphere above granulation near plages could also contribute to brighter contrast references in the AR FOVs.

To check this possibility, we compared the (intensity) "instrumental data number" values (i.e. those of level 1 data obtained after calibration with `sp_prep`[5], cf. Sect. 2.2) of the contrast references $\langle I_{\rm c}\rangle_{\rm ref,FOV}$ used in the different FOVs, as plotted in Fig. 6. In addition to the effect mentioned above, the $\langle I_{\rm c}\rangle_{\rm ref,FOV}$ values can also vary due to oscillation-induced brightness fluctuations, possible differences in convection and instrumental variations from one scan to the next (for instance, varying amount of defocus, see Danilovic et al. 2008). All this leads to a scatter of the values with a rms of 1.2%. To look for a systematic difference between the QS and AR contrast references, we averaged those values and overplotted the averages of the QS and the AR $\langle I_{\rm c}\rangle_{\rm ref,FOV}$ as horizontal bars. As indicated by the right-hand side y-axis of the plot, the average of the $\langle I_{\rm c}\rangle_{\rm ref,FOV}$ of the AR FOVs is lower than the average value of the QS FOVs and differs by only -0.5 ± 0.2% (the error is the sum of the errors on the QS and AR averages). This is five times smaller and of opposite sign than the relative difference of 2.4% between the average peak contrasts in ARs and QS. We can thus rule out that the lower observed contrasts of magnetic elements in ARs compared to the QS are related to systematically brighter contrast reference areas in ARs.

3.5. Comparison with previous studies of contrast vs. magnetogram signal

Here we propose possible explanations as to why our trends of continuum contrast averaged in bins of apparent longitudinal field strength $B_{\rm app,los}$ peak at finite $B_{\rm app,los}$ in ARs, whereas the trends of Title et al. (1992); Topka et al. (1992); Lawrence et al. (1993) (TTL) in ARs decrease monotonically.

One source of discrepancy lies in the different pore removal techniques employed by TTL and by us. If instead of our pore

[5] For terminology, see the Hinode SOT Data Analysis Guide at http://solarwww.mtk.nao.ac.jp/katsukaw/sot_fits/SOT00042_C_SOT_Analysis_Guide_(SAG).pdf.

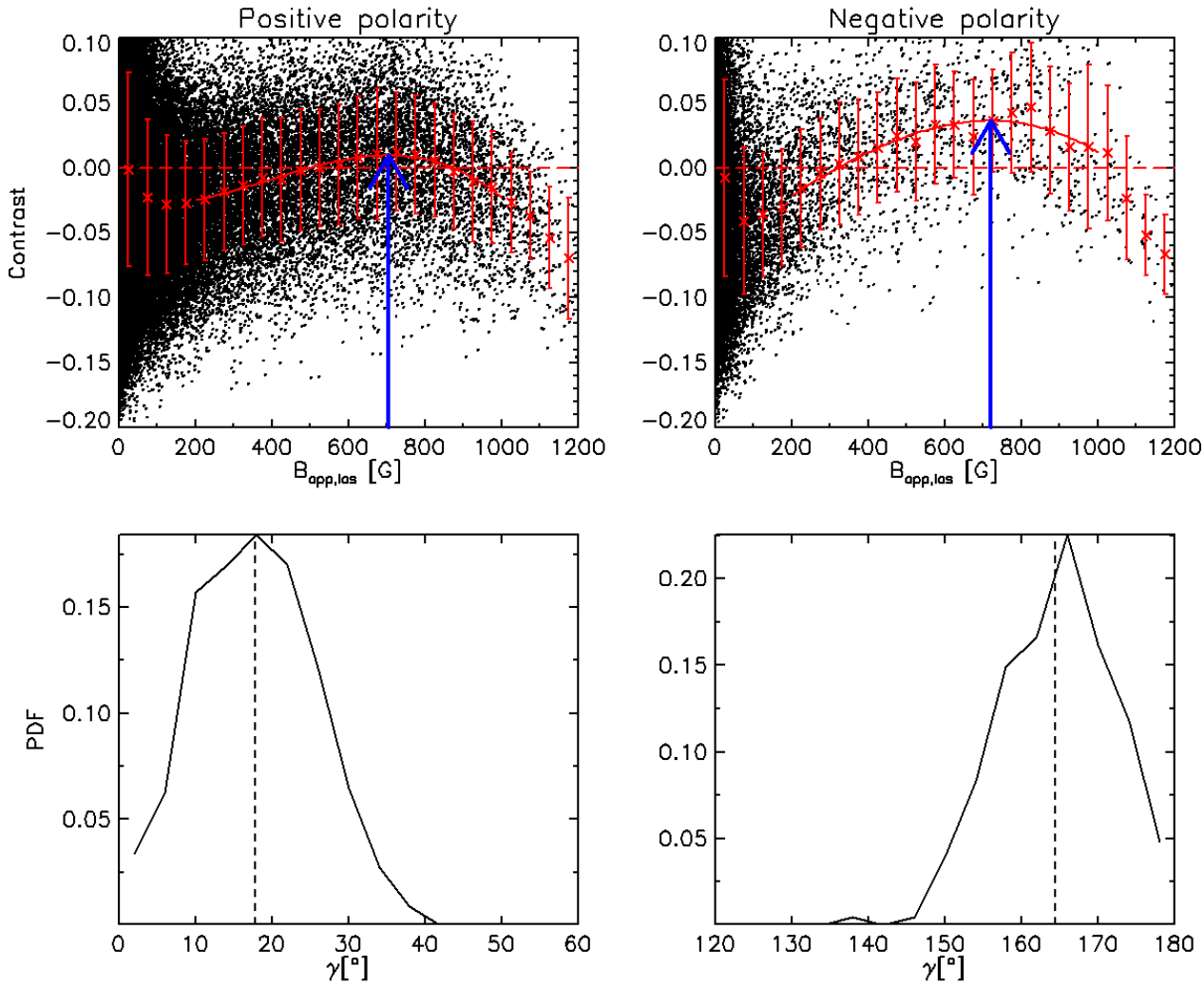

Fig. 5. *Upper panels*: scatterplot of continuum contrast vs. $B_{\rm app,los}$ for the positive and negative polarity in the FOV displayed in Fig. 4. Symbols are as in Fig. 2. *Lower panels*: probability distribution functions of the inclination γ retrieved by the inversion for the positive (between 0° and 90°) and negative (between 90° and 180°) polarity.

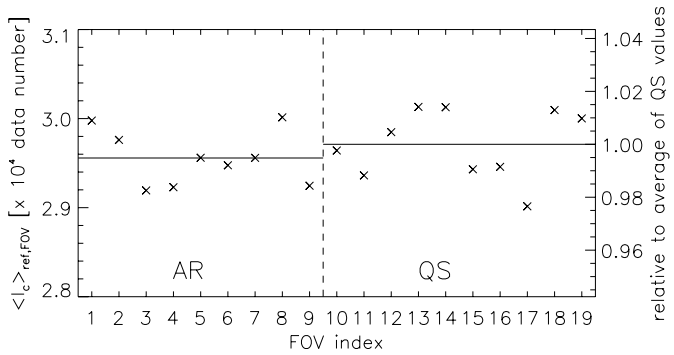

Fig. 6. Values of the contrast references $\langle I_{\rm c}\rangle_{\rm ref,FOV}$ used in the different AR and QS FOVs, in original data units. The FOV index labels the FOVs according to the order of Table 2. The horizontal bars represent the average values of the $\langle I_{\rm c}\rangle_{\rm ref,FOV}$ in the AR (left) and QS (right) FOVs. The right-hand side y axis gives the values relative to the QS average.

removal procedure, described in Sect. 3.1, we use a simple contrast threshold as employed by TTL on the plage FOV presented in Fig. 1, the resulting trend of the contrast vs. $B_{\rm app,los}$ is much flatter. For instance, by cutting out all the pixels with contrast below −0.18, we obtain the scatterplot displayed in Fig. 7 left panel, while our original pore removal leads to Fig. 2 lower panel[6]. The peak of the trend at 600–700 G is greatly reduced in Fig. 7 (the peak contrast reaches only −0.01 compared to 0.005 in Fig. 2), while the darkening at $B_{\rm app,los} > 800$ G is significantly enhanced. This is because a simple intensity cut only removes the inner dark cores of the pores, which mostly contribute to the range $B_{\rm app,los} > 800$ G. But our more-complex procedure also removes the immediate surroundings of the pores, where the pixels are darkened by the point spread function of the telescope. Such pixels typically provide contributions in the range 200–800 G and if not removed, tend to flatten the peak of the contrast curves. The effect of the telescope diffraction on the surroundings of the pores is illustrated by cuts of contrast and $B_{\rm app,los}$ across pores of different sizes, as plotted in Fig. 8. The cuts were extracted from the plage area of Fig. 1 where they are marked by thick white lines. On both sides of the dark cores (identified in the cuts as having contrast <−0.18 and marked by the long dashed lines in

[6] Note that due to different spatial resolutions and contrasts, we cannot use the same threshold values as TTL. The threshold value of −0.18 used here was chosen to be as high as possible without cutitng in intergranular lanes.

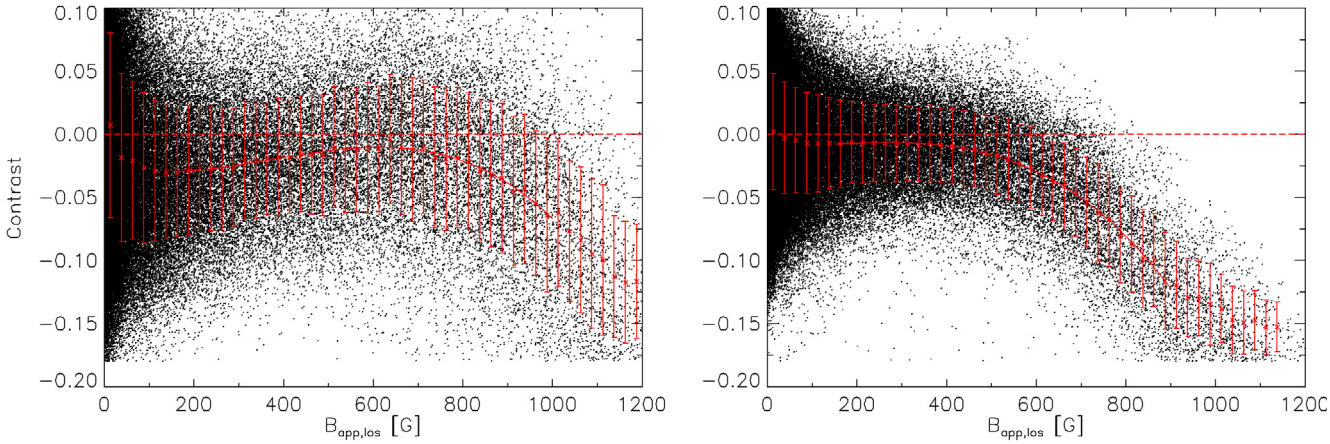

Fig. 7. *Left*: scatterplot of the continuum contrast vs. longitudinal flux density $B_{\rm app,los}$ for the plage field of view (FOV) shown in Fig. 1, obtained by removing the pores via a simple contrast threshold at a value of −0.18. *Right*: scatterplot of the continuum contrast vs. apparent longitudinal field strength $B_{\rm app,los}$ for the same plage FOV, obtained after degradation of the contrast and $B_{\rm app,los}$ by convolving with a Gaussian of *FWHM* 0.″45 and a Lorentzian of *FWHM* 0.″06 (mimicing straylight), while removing the pores with the same contrast threshold.

Fig. 8), we find several pixels where the contrast is slightly negative or neutral and $B_{\rm app,los} > 200$ G. To remove these pixels, our pore removal procedure extends the detected dark cores of pores (which we actually require to have contrasts <−0.15 *and* $B_{\rm app,los} > 900$ G, see Sect. 3.1) until $B_{\rm app,los}$ drops below 200 G. The boundaries obtained in this manner are marked by short-dashed lines in Fig. 8.

To reproduce a monotonically decreasing contrast curve like the ones of TTL, we also had to degrade our data. These authors indeed state that the spatial resolution is at best 0.″3 and 0.″45 for their images and magnetograms, respectively. We obtained a good match to TTL's results if we degraded *both* the continuum images and Stokes images with a Gaussian of 0.″45 *FWHM*, plus an additional Lorentzian degradation of 0.″06 *FWHM* to mimic straylight. This yielded the monotonically decreasing contrast trend of Fig. 7 right, provided the pores were eliminated via a simple intensity cut as described before[7]. Although the Gaussian degradation already reduces the contrast range to values similar to TTL's, the additional Lorentzian degradation was needed in order to obtain such a monotonic decrease. The width of that Lorentzian was adjusted so that the rms contrast calculated in a 20″ box of quiet Sun in our images matches the one given by Topka et al. (1992) (6% at 558 nm, corresponding to about 5% at 630 nm). This additional degradation implies that TTL's results are probably sgnificantly influenced by straylight, which is very typical for ground-based observations. In contrast, the small amount of scattered light in Hinode's spectropolarimeter (Danilovic et al. 2008) can be neglected. However, we warn against inferring that the *FWHM* of our degradations corresponds to the actual resolution of TTL. As will be shown in a second paper (Kobel et al., in prep.), the shape and peak value of the contrast vs. $B_{\rm app,los}$ trend also depend on the amount of flux contained in the FOV.

That the spatial resolution is an important factor influencing the peak of the contrast curves can also be seen by comparing with the more recent studies of Berger et al. (2007) and Narayan & Scharmer (2010), using higher resolution (0.″15) SST data consisting in 630.2 nm magnetograms, together with *G*-band and 630.2 nm continuum filtergrams, respectively (exclusively in ARs). Using the same pixel-by-pixel method as us, both groups of authors found a peak contrast reaching up to 2–3% (of the mean intensity in the FOV) in the study of Narayan & Scharmer (2010) and 3–4% in the case of Berger et al. (2007). The latter study, however, is not directly comparable since magnetic elements are known to exhibit enhanced contrasts in *G*-band (e.g. Muller & Roudier 1984). Future studies at higher resolution and lower straylight thus promise to reach even higher contrasts (e.g. with the SUNRISE balloon-borne observatory Barthol et al. 2011; Solanki et al. 2010; Riethmüller et al. 2010). Note that in spite of his much lower spatial resolution (magnetograph aperture of 2.″4), Frazier (1971) did find peaked contrast curves in two active regions. According to the above, we can possibly attribute this to a lower amount of straylight (compared to TTL), the presence of only a few pores in his field of view, or a lower degree of magnetic activity.

4. Discussion and conclusion

Owing to its better spatial resolution and its low amount of scattered light, Hinode/SP allowed us to update the results of earlier ground-based studies of continuum contrast vs. magnetogram signal (Title et al. 1992; Topka et al. 1992, 1997; Lawrence et al. 1993, referred to in this paper as TTL) in the QS and in ARs. In agreement with the previous finding of Lawrence et al. (1993), the contrasts reach larger values in the QS than in ARs, with a relative contrast difference of 2.5% (average over 8 and 10 fields of view in ARs and the QS, respectively). This difference could not be attributed to any brightness enhancement of the reference areas in ARs (see Sect. 3.4), so that it likely relates to an intrinsic brightness difference between the brightest magnetic elements in ARs and in the QS. Whereas TTL were finding monotonically decreasing trends in ARs, the trends of the contrast vs. (apparent) longitudinal field strength $B_{\rm app,los}$ now display a clear peak *both* in ARs and in the QS, as visible in Fig. 7. We explained our peak in ARs by the higher spatial resolution and low amount of straylight of Hinode compared with the earlier ground-based observations of TTL, as well as by our removal of the pores and the part of their close surroundings affected by the telescope diffraction (tending to smear the contrast curve). This contrast peak enables us to attribute an apparent longitudinal field strength value to the

[7] If before the degradation we eliminate the pores with our own pore removal procedure, the resulting curve (not shown here) still exhibits a peak.

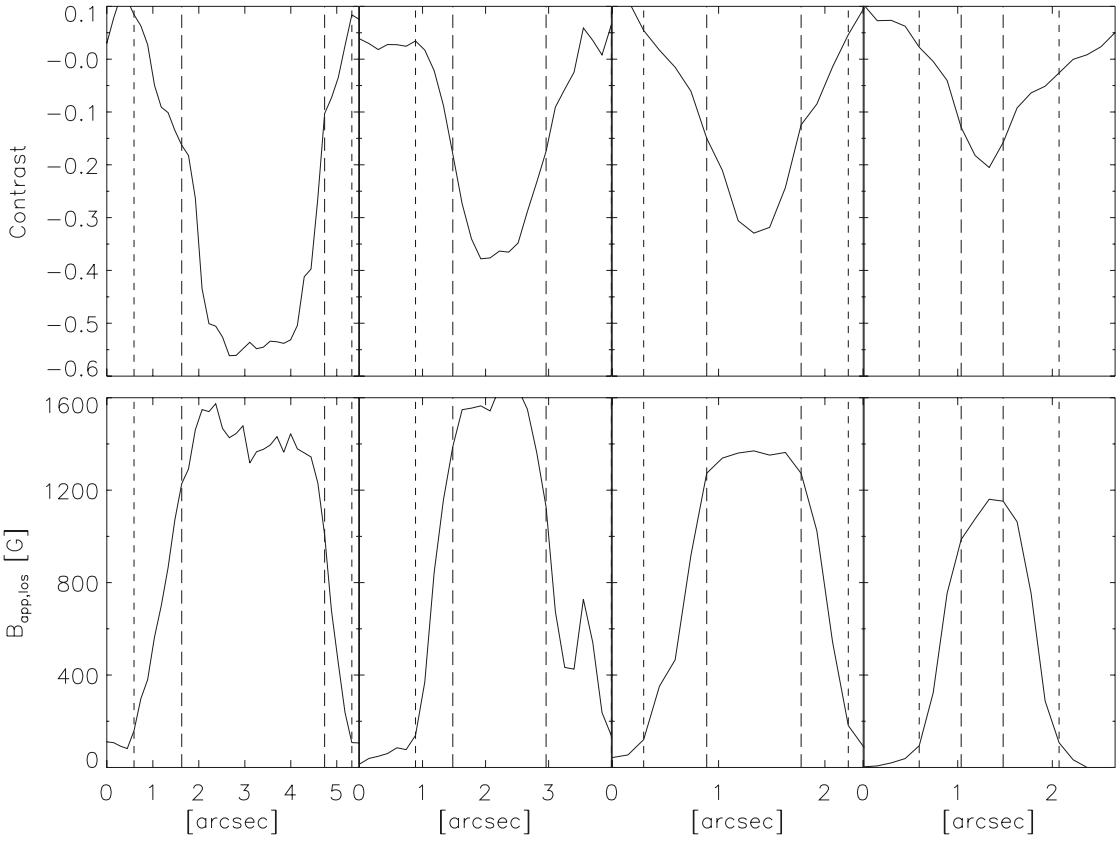

Fig. 8. Contrast (*upper panels*) and $B_{app,los}$ (*lower panels*) cuts across four pores of decreasing size. The pixels located between the long dashed lines have contrasts inferior to −0.18, and the short dashed lines enclose the pixels having $B_{app,los} > 200$ G. Note that due to the pixellation of the profiles, the vertical dashed lines do not cross them exactly at those values. All cuts have been extracted from the plage field of view shown in Fig. 1 and their locations are indicated in that figure by white solid lines.

brightest pixels in ARs and QS. Interestingly, the apparent longitudinal field strength corresponding to the peak contrast is similar for ARs and QS, $B_{app,los} \sim 700$ G. Note that the continuum contrast curve of Narayan & Scharmer (2010, Fig. 2 upper right panel) also peaks at $B_{app,los} \sim 700$ G, although they used data from the Swedish Solar Telescope (SST). Given the theoretically factor of 2 higher spatial resolution of SST compared to Hinode, this is surprising in the light of recent tests with degraded MHD simulation snapshots. These indicate that the presence of a peak as well as its associated $B_{app,los}$ value depend on the spatial resolution (Röhrbein & Schüssler in prep.)[8]. However, as mentioned by Narayan & Scharmer (2010), it is likely that their $B_{app,los}$ are underestimated due to instrumental and seeing-induced stray-light. This may explain the similar $B_{app,los}$ of the peak. In this respect, it would be interesting to determine the contrasts of BPs in ARs at still higher spatial resolution, as afforded by SUNRISE (Barthol et al. 2011), should appropriate data become available from a future flight.

We checked that the pixels contributing to the contrast peak (i.e. with $B_{app,los}$ around 700 G) are mainly located in intergranular lanes (cf. Fig. 1) and can thus be reasonably associated with magnetic elements. From the inversions we found that for these pixels the intrinsic magnetic field is kG in strength and rather vertical (as expected for magnetic elements), as shown in Fig. 3a,b. Consequently, the magnetic elements with higher continuum contrasts also share similar filling factors in ARs and in the QS (see Fig. 3c), which poses the problem of how to interpret their larger brightness in the QS.

It can be argued that at Hinode's spatial resolution it is unlikely that many flux tubes are present in a pixel, and consequently that the filling factor in most cases reflects the size of the (unresolved) magnetic elements. This is supported by recent results obtained with SUNRISE/IMaX (spatial resolution between 0.″15 and 0.″18, Martinez Pillet et al. 2010) concluding that many of the QS magnetic elements were spatially resolved (Lagg et al. 2010) even in the internetwork. Since the resolution of Hinode/SP is only a factor of 2 inferior (∼0.″3), it must be close to resolving them, although we cannot rule out that even smaller kG features are present. Under the assumption of a single magnetic elements per pixel on average, one could deduce that the brightest magnetic elements have similar sizes in ARs and in the QS in spite of their different brightness, which in turn questions the conventional interpretation that the brightness of magnetic elements is primarily dictated by their size.

The only inversion parameter studied here that slightly differs between the brightest magnetic elements in ARs and in the QS is the inclination, which is on average 5° larger in ARs (see Fig. 3c and Table 2). However, we cannot think of any physical argument explaining why more inclined magnetic elements appear darker. Rather, inclined flux tubes should appear brighter as their hot walls is more exposed to a vertical line-of-sight (as proposed by Topka et al. 1992). We think that the more inclined fields in ARs are just a consequence of the presence of pores and dense groups of flux tubes exerting a bending force on the field lines of magnetic elements located at their periphery (due to the

[8] For original snapshots of simulations with $\langle B \rangle$ up to 200 G, the bolometric intensity increases with B (see also Vögler et al. 2005) but shows a peak after degradation.

solenoidality of the magnetic field and the expansion of the flux tubes with height).

Another factor that influences the heating of the magnetic elements is the efficiency of the surrounding convection. It is well-known that the number density of magnetic elements (and thereby the average filling factor) is higher in AR plages than in the QS network, and the "degree of packing" of magnetic elements is likely to affect the surrounding convective motions (as first suggested by Knölker et al. 1988). Morinaga et al. (2008) recently found (using Hinode observations of a pore and its surrounding plage) that the disperion in line-of-sight velocity was smaller in regions of larger averaged filling factor, while Ishikawa et al. (2008) also observed reduced convective velocities in regions of high apparent longitudinal field. This could also explain why the minority polarity magnetic elements in ARs, which are less densely packed and form smaller patches, reach larger contrasts (in the few cases investigated in Sect. 3.3). A systematic study of whether the degree of inhibition of convection relates to the brightness of magnetic elements will be presented in a second paper (Kobel et al., in prep.).

Acknowledgements. We gratefully thank M. Schüssler, D. Rörbein, B. Viticchié, Y. Unruh, J. Sanchez-Almeida and the ground-based solar observation group at the Max-Planck Institut für Sonnensystemforschung for interesting discussions about this work. This work has been partially supported by WCU grant No. R31-10016 funded by the Korean Ministry of Education Science and Technology. Hinode is a Japanese mission developed and launched by ISAS/JAXA, collaborating with NAOJ, NASA and STFC (UK). Scientific operation of the Hinode mission is conducted by the Hinode science team organized at ISAS/JAXA. This team mainly consists of scientists from institutes in the partner countries. Support for the post-launch operation is provided by JAXA and NAOJ (Japan), STFC (UK), NASA, ESA, and NSC (Norway). This work has also made use of the NASA ADS database.

References

Barthol, P., Gandorfer, A., Solanki, S. K., et al. 2011, Sol. Phys., 268, 1
Berger, T. E., & Title, A. M. 1996, ApJ, 463, 365
Berger, T. E., & Title, A. M. 2001, ApJ, 553, 449
Berger, T. E., Löfdahl, M. G., Shine, R. S., & Title, A. M. 1998, ApJ, 495, 973
Berger, T. E., Rouppe van der Voort, L., & Löfdahl, M. 2007, ApJ, 661, 1272
Borrero, J. M., & Kobel, P. 2011, A&A, 527, A29
Borrero, J. M., Tomczyk, S., Kubo, M., et al. 2010, Sol. Phys., 35
Brooks, D. H., Kurokawa, H., & Berger, T. E. 2007, ApJ, 656, 1197
Danilovic, S., Gandorfer, A., Lagg, A., et al. 2008, A&A, 484, L17
De Pontieu, B., Carlsson, M., Stein, R., et al. 2006, ApJ, 646, 1405
Deinzer, W., Hensler, G., Schussler, M., & Weisshaar, E. 1984, A&A, 139, 435
del Toro Iniesta, J. C. 2003, Introduction to Spectropolarimetry (Cambridge, UK: Cambridge University Press)
Domingo, V., Ermolli, I., Fox, P., et al. 2009, Space Sci. Rev., 145, 337
Frazier, E. N. 1971, Sol. Phys., 21, 42
Frazier, E. N., & Stenflo, J. O. 1972, Sol. Phys., 27, 330
Hirzberger, J., & Wiehr, E. 2005, A&A, 438, 1059
Howard, R., & Stenflo, J. O. 1972, Sol. Phys., 22, 402
Ichimoto, K., Lites, B., Elmore, D., et al. 2008, Sol. Phys., 249, 233
Ishikawa, R., & Tsuneta, S. 2009, A&A, 495, 607
Ishikawa, R., Tsuneta, S., Ichimoto, K., et al. 2008, A&A, 481, L25
Keller, C. U., Schüssler, M., Vögler, A., & Zakharov, V. 2004, ApJ, 607, L59
Khomenko, E. V., Collados, M., Solanki, S. K., Lagg, A., & Trujillo Bueno, J. 2003, A&A, 408, 1115
Knölker, M., Schüssler, M., & Weisshaar, E. 1988, A&A, 194, 257
Knölker, M., Grossmann-Doerth, U., Schüssler, M., & Weisshaar, E. 1991, Adv. Space Res., 11, 285
Kobel, P., Hirzberger, J., Solanki, S. K., Gandorfer, A., & Zakharov, V. 2009, A&A, 502, 303
Komm, R. W., Howard, R. F., & Harvey, J. W. 1993, Sol. Phys., 147, 207
Kosugi, T., Matsuzaki, K., Sakao, T., et al. 2007, Sol. Phys., 243, 3
Krivova, N. A., Solanki, S. K., Fligge, M., & Unruh, Y. C. 2003, A&A, 399, L1
Krivova, N. A., Solanki, S. K., & Floyd, L. 2006, A&A, 452, 631
Krivova, N. A., Balmaceda, L., & Solanki, S. K. 2007, A&A, 467, 335
Lagg, A., Solanki, S. K., Riethmüller, T. L., et al. 2010, ApJ, 723, L164
Landi Degl'Innocenti, E., & Landolfi, M. 2004, Polarization in Spectral Lines, Astrophys. Space Sci. Lib., 307
Lawrence, J. K., Topka, K. P., & Jones, H. P. 1993, J. Geophys. Res., 98, 18911
Lin, H. 1995, ApJ, 446, 421
Lites, B. W. 2002, ApJ, 573, 431
Lites, B. W., Elmore, D. F., & Streander, K. V. 2001, in Advanced Solar Polarimetry – Theory, Observation, and Instrumentation, ed. M. Sigwarth, ASP Conf. Ser., 236, 33
Lites, B. W., Scharmer, G. B., Berger, T. E., & Title, A. M. 2004, Sol. Phys., 221, 65
Lites, B. W., Kubo, M., Socas-Navarro, H., et al. 2008, ApJ, 672, 1237
Martinez Pillet, V., del Toro Iniesta, J. C., Alvarez-Herrero, A., et al. 2010, Sol. Phys., in press
Morinaga, S., Sakurai, T., Ichimoto, K., et al. 2008, A&A, 481, L29
Muller, R., & Roudier, T. 1984, Sol. Phys., 94, 33
Narayan, G., & Scharmer, G. B. 2010, A&A, 524, A3
Neckel, H., & Labs, D. 1994, Sol. Phys., 153, 91
Orozco Suárez, D., Bellot Rubio, L. R., Del Toro Iniesta, J. C., et al. 2007, PASJ, 59, 837
Rabin, D. 1992a, ApJ, 390, L103
Rabin, D. 1992b, ApJ, 391, 832
Rempel, M. 2006, ApJ, 647, 662
Riethmüller, T. L., Solanki, S. K., Martínez Pillet, V., et al. 2010, ApJ, 723, L169
Schnerr, R. S., & Spruit, H. C. 2011, A&A, submitted [arXiv:1010.4792]
Schüssler, M. 1992, in The Sun: A Laboratory for Astrophysics, ed. J. T. Schmelz, & J. C. Brown, NATO Advanced Study Institute Series C Proc., 373, 191
Schuessler, M., & Solanki, S. K. 1988, A&A, 192, 338
Sheeley, Jr., N. R. 1969, Sol. Phys., 9, 347
Solanki, S. K. 1993, Space Sci. Rev., 63, 1
Solanki, S. K., & Stenflo, J. O. 1984, A&A, 140, 185
Solanki, S. K., Zufferey, D., Lin, H., Rüedi, I., & Kuhn, J. R. 1996, A&A, 310, L33
Solanki, S. K., Inhester, B., & Schüssler, M. 2006, Rep. Prog. Phys., 69, 563
Solanki, S. K., Barthol, P., Danilovic, S., et al. 2010, ApJ, 723, L127
Spruit, H. C. 1976, Sol. Phys., 50, 269
Spruit, H. C. 2003, Sol. Phys., 213, 1
Spruit, H. C., & Zwaan, C. 1981, Sol. Phys., 70, 207
Steiner, O. 2005, A&A, 430, 691
Steiner, O. 2007, in Modern Solar Facilities – Advanced Solar Science, ed. F. Kneer, K. G. Puschmann, & A. D. Wittmann (Universitätsverlag Göttingen), 321
Stenflo, J. O. 1973, Sol. Phys., 32, 41
Stenflo, J. O. 2008, J. Astrophys. Astron., 29, 19
Stenflo, J. O., & Harvey, J. W. 1985, Sol. Phys., 95, 99
Suematsu, Y., Tsuneta, S., Ichimoto, K., et al. 2008, Sol. Phys., 249, 197
Title, A. M., & Berger, T. E. 1996, ApJ, 463, 797
Title, A. M., Tarbell, T. D., Topka, K. P., et al. 1989, ApJ, 336, 475
Title, A. M., Topka, K. P., Tarbell, T. D., et al. 1992, ApJ, 393, 782
Topka, K. P., Tarbell, T. D., & Title, A. M. 1992, ApJ, 396, 351
Topka, K. P., Tarbell, T. D., & Title, A. M. 1997, ApJ, 484, 479
Tsuneta, S., Ichimoto, K., Katsukawa, Y., et al. 2008, Sol. Phys., 249, 167
Uitenbroek, H., & Tritschler, A. 2006, ApJ, 639, 525
Viticchié, B., Del Moro, D., Criscuoli, S., & Berrilli, F. 2010, ApJ, 723, 787
Vögler, A., & Schüssler, M. 2003, Astronom. Nachr., 324, 399
Vögler, A., Shelyag, S., Schüssler, M., et al. 2005, A&A, 429, 335
Walton, S. R., Preminger, D. G., & Chapman, G. A. 2003, ApJ, 590, 1088
Zakharov, V., Gandorfer, A., Solanki, S. K., & Löfdahl, M. 2007, A&A, 461, 695
Zayer, I., Stenflo, J. O., Keller, C. U., & Solanki, S. K. 1990, A&A, 239, 356
Zhao, J., & Kosovichev, A. G. 2004, ApJ, 603, 776